Enhanced Solar-to-Hydrogen Generation with Broadband Epsilon-Near-Zero Nanostructured Photocatalysts

Yi Tian, Francisco Pelayo García de Arquer, Cao-Thang Dinh, Gael Favraud, Marcella Bonifazi, Jun Li, Min Liu, Xixiang Zhang, Xueli Zheng, Md. Golam Kibria, Sjoerd Hoogland, David Sinton, Edward H. Sargent, and Andrea Fratalocchi**

The direct conversion of solar energy into fuels or feedstock is an attractive approach to address increasing demand of renewable energy sources. Photocatalytic systems relying on the direct photoexcitation of metals have been explored to this end, a strategy that exploits the decay of plasmonic resonances into hot carriers. An efficient hot carrier generation and collection requires, ideally, their generation to be enclosed within few tens of nanometers at the metal interface, but it is challenging to achieve this across the broadband solar spectrum. Here the authors demonstrate a new photocatalyst for hydrogen evolution based on metal epsilon-near-zero metamaterials. The authors have designed these to achieve broadband strong light confinement at the metal interface across the entire solar spectrum. Using electron energy loss spectroscopy, the authors prove that hot carriers are generated in a broadband fashion within 10 nm in this system. The resulting photocatalyst achieves a hydrogen production rate of 9.5 µmol h^{-1} cm^{-2} that exceeds, by a factor of 3.2, that of the best previously reported plasmonic-based photocatalysts for the dissociation of H_2 with 50 h stable operation.

Photocatalytic production of hydrogen is a promising route to convert solar energy into fuels and chemical feedstocks. The approach consists of a photoactive material, typically a semiconductor, which harvests and then transfers solar electrons to catalytic sites to drive hydrogen evolution reaction.[1–4] Direct photoexcitation of metals has emerged in recent years as an attractive strategy for hydrogen generation.[5,6] In contrast with the case of semiconductors, this approach relies on the strong light-matter interaction in nanostructured metals to couple incident light into plasmonic resonances. These intense modes can be readily tuned by modifying the metal environment and morphology.[7] Under appropriate conditions, photogenerated plasmons decay into a population of nonequilibrium high-energy carriers (Landau-damping) that can be used to drive chemical reactions.[8] Intense efforts have been devoted in recent years to understand and optimize the mechanisms underlying behind this process both from an optoelectronic[9–13] and a catalytic perspective.[14–20]

The efficient usage of hot carriers requires their rapid extraction in order to surmount their ultrafast relaxation dynamics, the latter occurring in the sub-ps regime.[21–23] Strategies to improve the hot carrier generation rate and the collection efficiency have been devised. Theory and experiments support that, to maximize hot carrier harvesting, their generation needs to be tightly confined to small volumes, below few tens of nanometers, to the metal interface.[24–27]

It is of paramount importance to utilize the high tunability endowed by plasmonic systems to achieve broadband hot carrier harvesters. Efforts in this direction have thus far included the use of nanoantennas,[9] nanorods,[18] and plasmonic crystals[27] to achieve multispectral features. A single material platform that tightly concentrates hot carrier generation to the metal interface and that does so in a broadband fashion across the solar spectrum, is required to exploit the potential of photoexcited metal-driven catalysis.

Here we propose a new strategy to achieve highly efficient photocatalysis in a material based on 3D epsilon-near-zero (ENZ) nanostructures. ENZ metamaterials are optical structures whose properties emerge as the refractive index of the structure approaches zero.[28–32] These properties can be used to slow down light dramatically, concentrating it on nanometric dimensions. We designed broadband ENZ materials based on fractal metallic nanostructured needles and implemented them in a $Pd/TiO_2/Pt$ heterojunction. Using electron energy loss

Y. Tian, Dr. G. Favraud, M. Bonifazi, Prof. A. Fratalocchi
PRIMALIGHT
Faculty of Electrical Engineering
Applied Mathematics and Computational Science
King Abdullah University of Science and Technology (KAUST)
Thuwal 23955-6900, Saudi Arabia
E-mail: andrea.fratalocchi@kaust.edu.sa
Dr. F. P. García de Arquer, Dr. C.-T. Dinh, Dr. M. Liu, Dr. X. Zheng, Dr. Md. G. Kibria, Dr. S. Hoogland, Prof. E. H. Sargent
Department of Electrical and Computer Engineering
University of Toronto
35 St. George Street, Toronto, Ontario M5S 1A4, Canada
E-mail: ted.sargent@utoronto.ca
Prof. D. Sinton
Department of Mechanical and Industrial Engineering
University of Toronto
5 Kings College Road, Toronto, Ontario M5S 3G8, Canada
Dr. J. Li, Prof. X. Zhang
Division of Physical Science and Engineering
King Abdullah University of Science and Technology
Thuwal 239955, Saudi Arabia

DOI: 10.1002/adma.201701165

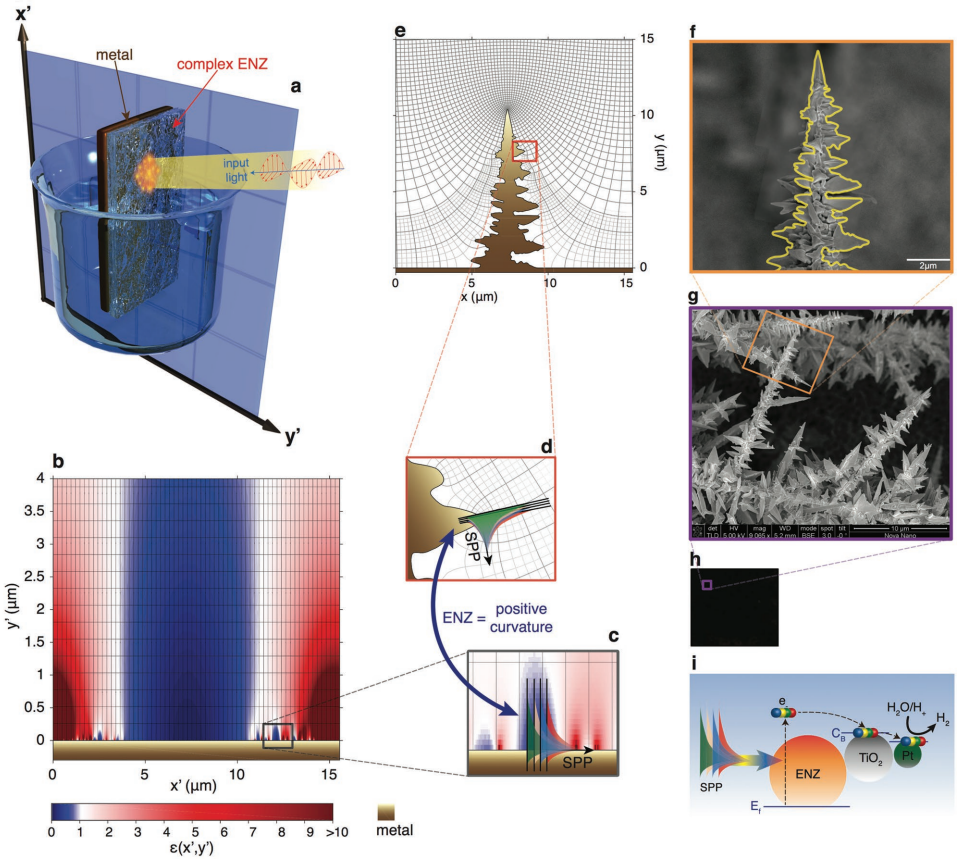

Figure 1. Broadband ENZ plasmonic photocatalysis: general idea and sample fabrication. a) Schematic illustration of a freestanding ENZ photocatalyst material. b) Optical properties of the complex ENZ structure along the (x', y') plane. ENZ regions are illustrated in dark blue color. c) Zoomed detail of (b), showing the motion of SPP waves excited by the light-matter interaction with impinging broadband photons. d,e) The equivalent structures of panels (b) and (c), respectively, calculated by applying transformation optics. Panel (d) also shows the corresponding broadband squeezing of light in the points of positive curvatures of the material, where the equivalent ENZ regions exist. f) STEM image of a fabricated sample, with a 2D cross-section in yellow representing the structure of panel (e). g) SEM image and h) naked eye image of the sample. i) Broadband ENZ plasmonic photocatalysis reaction diagram.

spectroscopy, we demonstrate that hot carrier generation occurs in a broadband fashion in sub 10 nm dimensions. The ENZ $Pd/TiO_2/Pt$ photocatalyst shows stable solar-to-hydrogen generation over 50 h, providing an avenue to renewable production of H_2 on large scales.

Figure 1a illustrates the concept of the complex ENZ structure. The design incorporates a layer of an ENZ material atop a planar metallic substrate, which acts as an electron reservoir (Figure 1a). Figure 1b shows a section of the refractive index of the structure. The system is composed of a flat metallic surface covered by a material with a permittivity $\varepsilon(x', y')$, characterized by a network of ENZ regions separated by areas of high refractive index. The permittivity $\varepsilon(x', y')$ does not change in frequency, i.e., it is dispersionless. When photons impinge on this structure, surface plasmon polaritons (SPP) waves are generated at different wavelengths and propagate at the metal-dielectric interface $y' = 0$ (Figure 1c, SPP waves with different colors). When light waves enter into an ENZ region, the wave frequency diverges and electromagnetic energy is arrested inside the ENZ volume, generating a strong quasi-static localization.[28] Due to the dispersionless nature of the electromagnetic response of the complex ENZ material, SPP waves propagating at different frequencies become trapped inside the ENZ regions (Figure 1c), and these behave as wideband absorbers that confine light into localized volumes. This is key for the enhanced production of hot carriers in the system. The density of hot carriers generated in a plasmonic material illuminated by an electromagnetic wave, in fact, is proportional to the electric field intensity.[23–25,33] The broadband squeezing of light observed in Figure 1c results in a high electromagnetic intensity that, in turn, favors the decay of broadband SPP waves into highly energetic carriers. Even when SPP decayed radiatively, the broadband ENZ material traps the generated light until this energy is absorbed inside the metal, resulting in hot carrier generation.

When the ENZ material of Figure 1a–c is combined with a TiO_2 semiconductor and a Pt cocatalyst (Figure 1i), generated hot carriers are injected into the Pt catalyst wherein electrons reduce H_2O to H_2. The complex ENZ structure of Figure 1a–c provides a performance superior to that of conventional plasmonic structures. The latter are resonant and trap light efficiently only at specific wavelengths, for they lack of a mechanism for broadband light concentration.

The wide spectral character of the ENZ material is beneficial to solar absorption. It is not achieved using conventional

structures, since they possess at most one point in the spectrum at which the dielectric constant approaches zero. To overcome this problem, we followed the approach pioneered in refs. [34,35], and, by using transformation optics[36–38] we engineered a new material that is fully equivalent to that of Figure 1b,c and that can be easily fabricated on large scales. Transformation optics show that a planar metallic structure with an ENZ dielectric material on top is fully equivalent to a metallic surface with a convex curvature in air, while dielectric regions of high refractive index are equivalent to negative curvatures. This equivalence is a result of Maxwell equations that is demonstrated in ref. [35]. A detailed derivation of this transformation is also provided in Figure S1 of the Supporting Information for completeness. Figure 1d,e shows the equivalent medium of Figure 1b,c, respectively. In the transformed material of Figure 1d, the broadband localization effect is observed in each region of positive curvature, where SPP waves of different colors accumulate and where the equivalent ENZ material exists. Figure S3 of the Supporting Information shows how ENZ regions map on the equivalent structure of Figure 1d, providing a visual illustration of the spatial distribution of ENZ regions.

Figure S2 in the Supporting Information provides more details on the mechanism by which SPP waves are excited at the metal interface in the complex ENZ network material. Figure S1a in the Supporting Information shows a sample geometry composed of a complex ENZ nanomaterial, terminated by a flat metallic plane in air. The ENZ network structure is defined in the (x', y') coordinates. Figure S1b in the Supporting Information reports the equivalent metallic structure in the (x, y) space, calculated by transformation optics. In these coordinates space, the ENZ material is seen by light as a series of metallic nanostructures, with different shapes and curvatures, immersed in air. Figure S1c in the Supporting Information shows results of finite-different time-domain (FDTD) simulation in the (x, y) space when monochromatic light at the wavelength of $\lambda = 900$ nm impinges on the ENZ region (Figure S1b of the Supporting Information, green arrow). As seen from the figure, the complex light–matter interaction with the nanostructures generates a train of SPP waves, which are clearly visible and propagates in the flat metallic region after the termination of the nanostructures. Figure S1d in the Supporting Information illustrates the equivalent electromagnetic dynamics in the transformed (x', y') space. The excitation of SPP waves from the complex ENZ material from the fact that the ENZ network, being characterized by a random refractive index distribution with high and low refractive index values, behaves as a random grating that furnishes the required momentum to couple energy from incoming light to SPP waves. The article[35] provides more details on the mechanisms of excitation of SPP in these complex ENZ materials and how an accurate control of their localization can be attained at the metallic surface.

To fabricate the disordered structure profile illustrated in Figure 1e, we employ an electroplating technique, a scalable manufacturing method that has been successfully applied in biological sensing.[39,40] Disordered samples are fabricated by employing a three electrode potentiostat in a gold chloride solution ($HAuCl_4$), where the disordered metallic features are formed by the reduction of Au atoms on a flat substrate. The disordered system is then conformally coated with a 30 nm layer of palladium. Scanning electron microscope (SEM) images of a fabricated sample reveal a complex 3D Au/Pd metallic structure with a large number of convex substructures that theory predict will function as ENZ regions (Figure 1f) (details on the fabrication process are given in Experimental Section). Figure 1g shows a zoomed out SEM image of the sample, revealing a complex, fractal-like, pattern. Figure 1h shows the metallic sample as it appears to the naked eye: the structure is black. Its absorption exceeds 90% over the spectral range of 300–1300 nm (Figure S4, Supporting Information). Figure 1f–h illustrates the beneficial effect of disorder in this structure. The random character of the ENZ regions allows scalable electroplating fabrication and does not rely on prescriptive implementation of nanoscale features to result in a large number of convex curvatures. These act as equivalent ENZ regions for broadband light localization down to nanoscale regions where hot carrier generation is maximized. Figure S5 in the Supporting Information reports the absorption difference of samples characterized by Au and Au/Pd. The addition of a ultrathin layer of Pd, due to the higher absorption of Pd with respect to Au, allows to increase the overall absorption of the structure by 10%–15% in the near infrared window, allowing to collect more photons from impinging light.

In order to exploit efficiently the intense generation of hot carriers in the ENZ material, it is essential that we harness them before they thermalize. We used a Schottky junction to assist charge separation (Figure 1i): we employed TiO_2, a high-bandgap semiconductor that forms a Schottky junction with Pd, and possesses appropriate energetics to drive the hydrogen evolution reaction. It is also important to preserve the ENZ character of the metallic electrode along the steps involved in nanofabrication. Our assembly procedure employs low-temperature atomic layer deposition (ALD) that provides a uniform conformal coating and precise thickness control, implementing both a good Schottky junction and a protective layer for subsequent fabrication steps. Following 90 ALD cycles (≈8 nm), we applied a $TiCl_4$ densification and calcination treatments to the ENZ catalyst. This step has been reported to improve the crystallinity of the semiconducting phase and to remove potential organic residues from the underlying ALD coating. Samples were decorated with <10 nm Pt/C nanoparticles—a cocatalyst for hydrogen evolution—using a photoelectrochemical deposition procedure.

Figure 2a–e shows scanning transmission electron microscopy (STEM) images the final ENZ photocatalyst structure, including the complex $Pd/TiO_2/Pt$ heterojunction. The strategy ensures that ENZ features are preserved until the final catalyst is formed (Figure 2a). We confirmed the material composition of the ENZ catalyst by energy dispersive X-ray (EDX) spectroscopy (Figure 2b–e).

To experimentally demonstrate the broadband ENZ in our samples, we employ a combination of STEM and electron energy loss spectroscopy (EELS). STEM–EELS is an extremely powerful technique that allowed us to map, with nm resolution, the electromagnetic energy distribution within the ENZ network as experimentally measured from fabricated samples.[41,42]

Disordered samples used in STEM–EELS study were realized by employing the same deposition conditions for samples used

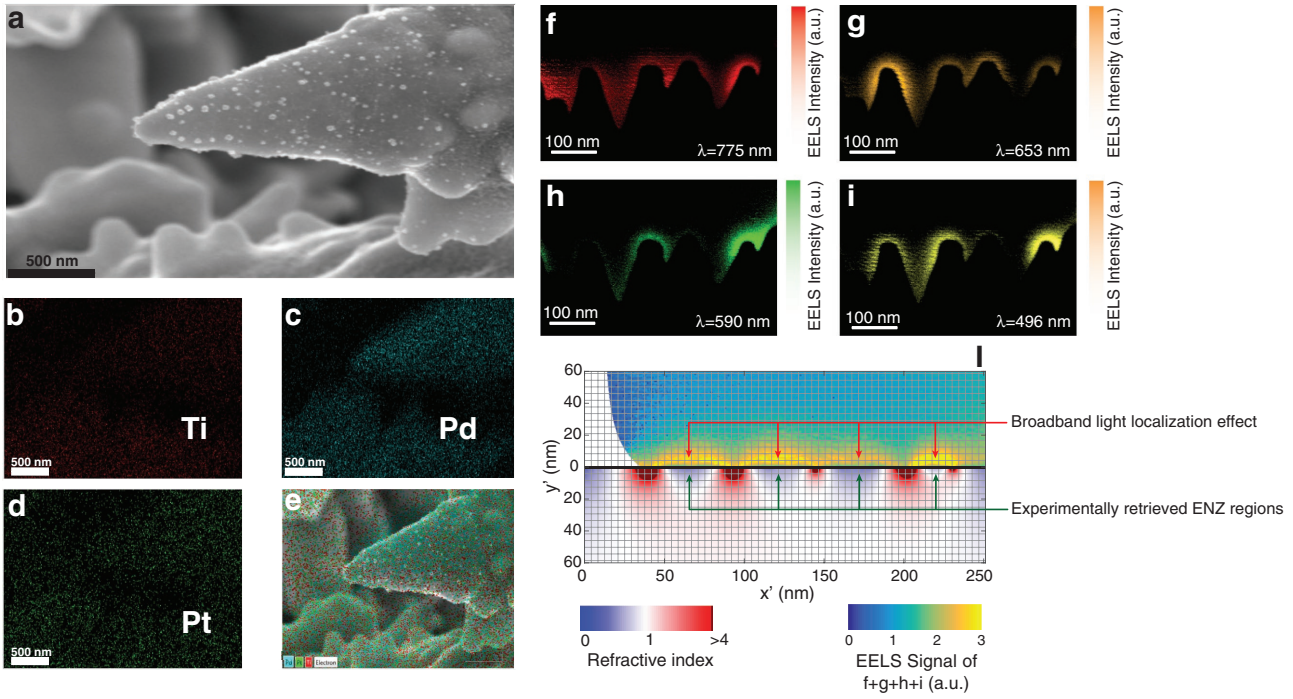

Figure 2. ENZ photocatalyst assembly and broadband experimental broadband ENZ effect demonstration by EELS. a) SEM image of a typical ENZ catalyst micron scale structure, consisting in a Pd metallic backbone coated with a TiO_2 layer decorated with Pt/C cocatalyst nanoparticles. After fabrication, the resulting photocatalyst material preserves the initial ENZ features. b–e) Energy dispersive X-ray (EDX) spectroscopy images of (b) Ti, (c) Pd, (d) Pt nanoparticles, with panel (e) superimposing (b–d) on the SEM image shown in panel (a). f–i) EELS plasmon mapping at 1.6, 1.9, 2.1, and 2.5 eV of nanoscale features of the complex ENZ material. l) Single image showing the results of panels (f–i) (EELS signal of f + g + h + i) and experimentally calculated refractive index distribution of ENZ regions (refractive index pseudocolor plot). Panel (l) experimentally proves a broadband ENZ effect where light is localized regardless of the input wavelength.

in photocatalysis experiments. To detect a measurable EELS signal in transmission, we required the metallic structure to be sufficiently thin to transmit electrons. We first sonicated the samples for 30 min in ethanol, and then deposited the resultant solution on a silicon substrate. This process allowed the complex metallic structures to detach away from the substrate while preserving their fractal shape. We then used focused ion beam scanning electron microscope (FIB-SEM) to cleave a single metallic tree-like structure and deposited it on a copper ring supporter for EELS analysis.

Figure 2f–i shows measured EELS spectra for different excitations ranging between 1.6 and 2.5 eV, which corresponds to wavelengths between λ = 496 and 775 nm. The spectral intensity of each pixel is imaged within a 0.2 eV energy window from the peak plasmonic energy, which is reported in the lower left panel of each picture. EELS plasmonic signals are presented in the figure with correlated light colors and shades that are proportional to the corresponding spectral intensity. The morphological information of the sample is observed in the black region under the colorful area in Figure 2f–i, corresponding to the metallic part of the sample. The distribution of electromagnetic energy measured by EELS on the sample under different input wavelengths and illustrated in Figure 2f–i is then mapped onto the refractive index distribution of the ENZ network in Figure 2i. To perform this mapping, we experimentally calculated the refractive index distribution of ENZ regions by extracting the morphology of the metallic surface of the sample. Figure S6 in the Supporting Information provides the details of this procedure. The resulting ENZ network is illustrated in Figure 2i as a pseudocolor map with varying shades between blue and red. The EELS electromagnetic field distribution is then represented in the same figure as a pseudocolor map with varying shades between dark blue and yellow. Figure 2i clearly proves experimentally the broadband ENZ effect of our samples. The image shows, in fact, broadband localization of the EELS signal in each ENZ region regardless of light frequency. From Figure 2i, we can estimate that the ENZ coverage is around 60% of the sample area.

The broadband light localization experimentally shown in Figure 2 is not the result of localized plasmonic resonances. The latter are observed in nanoparticles or equivalent resonant nanostructures that strongly interact with light at specific frequencies, which are dictated by their characteristic size.[43] Figure 2 also shows that each ENZ region supports a strong broadband localization effect, which does not exhibit any resonant character. The localization of light is the result of the trapping of SPP waves, which are excited at the surface by the mechanisms shown in Figure S2 of the Supporting Information and then get trapped in the complex ENZ network in the area of low refractive index, where light is arrested in broadband quasi-static localizations of strong electromagnetic intensity. The resulting material appears totally black, as our absorption experimental results show in Figure S4 (Supporting Information).

The theoretical study of hot carrier generation dynamics in metallic structures is a subject of debate.[23–25,33,44] Accurate theories exist so far only for simple geometries and lack for the complex structure of Figures 1 and 2. In order to provide physical insights on the performance of these structures, we use scaling laws for the generation of hot carriers obtained in ref. [24] that have been proven consistent with previous experiments.[23] According to Harutyunyan et al.,[23] at a given frequency ω the number of excited hot carriers $\mathrm{d}\mathcal{N}$ per unit energy $\mathrm{d}\mathcal{E}$ in a plasmonic material depends on the electromagnetic field intensity localized at the surface of the metal and is given by the following surface integral

$$\frac{\mathrm{d}\mathcal{N}(\omega)}{\mathrm{d}\mathcal{E}} = A\oint \frac{|\langle \mathbf{E}_n \rangle|^2}{\omega^4}\mathrm{dS} \quad (1)$$

being $\mathrm{d}S$ a unit surface element, $\langle \mathbf{E}_n \rangle$ the normal component of the electric field to the metallic/air interface averaged over one optical cycle at steady state, and A an inessential proportionality constant. In order to compute the relevant electromagnetic quantities to evaluate the performance of the ENZ structure from Equation (1), we used FDTD simulations on our homemade code NANOCPP, which provides very reliable results verified against numerous experiments.[45–47] To replicate the complex disorder arising in the ENZ samples, we used the structure of Figure 1e, whose morphology is extracted from SEM measurements.

Figure S7a in the Supporting Information shows the spatial distribution of the quantity $\delta\mathcal{N}(\mathbf{E}) = \int \mathrm{d}\omega \frac{|\langle \mathbf{E} \rangle|^2}{\omega^4}$, where $\mathbf{E}$ denotes the electric field. This function is proportional to the spatial distribution of the hot-electron generation rate, which according to Equation (1) is given by $\delta\mathcal{N}(\mathbf{E}_n)$ calculated at the metallic/air interface, apart inessential constants. For the computation of $\delta\mathcal{N}$ we illuminated the structure from the top with plane waves at different frequencies ω, we retrieve the corresponding average electric field intensity $|\langle \mathbf{E} \rangle|^2$ after the system reaches the steady state and then integrate over frequency space. In our computations we used a frequency illumination window between the wavelengths λ = 400 and 1000 nm, which span the visible and near infrared. To provide realistic computations, we used experimental dispersion curve of metals as measured from published experiments.[48]

The function $\delta\mathcal{N}$ illustrates that polychromatic light becomes squeezed in the ENZ regions formed at the points of positive curvature in the structure, generating a series of intense broadband light localizations that maximize hot carrier generation. Inside the ENZ regions, a second important mechanism that increases the flux of hot carriers comes from the propagation of surface plasmon waves, which tend to acquire an electric field perpendicular to the metallic surface (see the Supporting Information). This provides the desired scenario where electron momentum is matched and hot carrier emission is maximized.[23] Figure S7b in the Supporting Information provides a zoomed view of the distribution of the electric field inside and outside the metal (Figure S7b in the Supporting Information, pseudocolor plot). Electric field lines are plotted with a line integral convolution (LIC) technique that illustrates the vectorial distribution of the field in space (Figure S7b in the Supporting Information, quiver plot). The LIC plot clearly shows that the field becomes normal to the surface in the proximity of each ENZ region, where broadband light energy becomes squeezed.

Figure S7c in the Supporting Information calculates the hot carrier generation enhancement $\eta(\omega)$ obtained in the ENZ structure compared to a flat metallic control. For this calculation we evaluated Equation (1) for the disordered material and for a planar metallic sample between 400 and 1000 nm. The scaling $\frac{\mathrm{d}\mathcal{N}(\omega)}{\mathrm{d}\mathcal{E}} \propto 1/\omega^4$ in Equation (1) makes longer wavelength contributions more prominent. The result illustrated in Figure S7c in the Supporting Information shows that the photocatalyst enhances hot carrier generation rate in a broadband fashion. By integrating hot carrier density in frequency weighted by the spectrum of solar radiation (ω) (Figure S7c in the Supporting Information, solid area) we obtain an averaged enhancement factor $\bar{\eta}$ of ≈19, which reduces to 13 if we consider the presence of TiO_2, which provides an additional energy barrier of 1.2 eV, as estimated experimentally in the following text. This analysis predicts that the complex ENZ structure is expected to deliver a one order of magnitude improvement of hot carrier generation compared to conventional planar plasmonic structures. The analysis also shows that within the solar spectrum, light wavelengths >450 nm contribute more significantly to the enhancement η.

We assessed the photochemical reduction capabilities of the ENZ catalyst and connected as the working electrode in the electrochemical cell. We used Pt wire as a counter electrode, while Ag/AgCl in 3 M KCl was used as a reference (**Figure 3**a). Current voltammogram plots reveal the electrochemical activity of the ENZ as a cathode (Figure S8, Supporting Information). We biased the system at –0.1 V versus reversible hydrogen electrode (RHE) and monitored the current over time. A negative photocurrent is expected upon illumination if hydrogen H_2 is generated at the ENZ photocathode. Figure 3b confirmed this dynamics when the system is illuminated by periodically switched white light.

In the first set of measurements, we characterized the photoelectrical response of the ENZ photocathode under monochromatic illumination to obtain its photoelectrical external quantum efficiency spectrum (PEQE). This figure of merit is here used to calculate the value of the Schottky barrier at the Pd/TiO_2 interface. The external quantum efficiency is expressed as follows $\mathrm{PEQE} = \alpha \cdot \eta_{\mathrm{SPP\text{-}H_2}}$, where α denotes the absorption of the structure, $\eta_{\mathrm{SPP\text{-}H_2}}$ the total efficiency of hydrogen generation from photoexcited plasmons. This process includes the decay of SPPs into hot carriers, which propagate ballistically into the TiO_2 layer and react at the catalytic site to produce H_2. Figure 3c shows experimentally measured PEQE values for the ENZ photocatalyst in the visible and infrared spectrum. The emission process is often modeled following a Fowler theory. This trend follows well the Fowler prediction, with $\mathrm{PEQE} \propto \frac{(\hbar\omega - q\phi_b)^2}{\hbar\omega}$ and an estimation of $\psi_b \approx 1$ eV for the Schottky barrier.

Once we assessed the photoelectrochemistry of the ENZ catalyst, we characterized the complex ENZ heterostructure as a unit for photocatalytic H_2 generation. We placed the sample inside a sealed reactor with a mixture of water and MeOH, and subjected the system to AM 1.5G simulated illumination

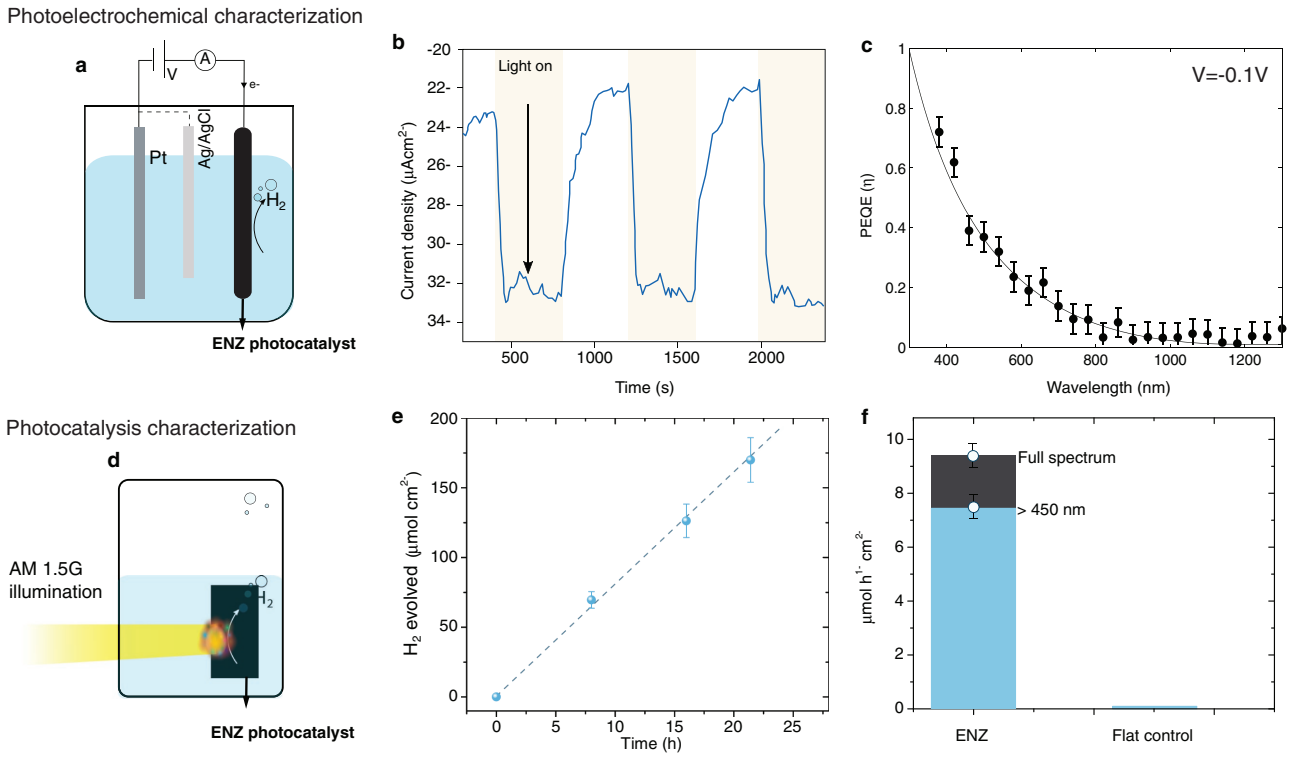

Figure 3. ENZ photocatalyst and hydrogen generation performance: photoelectrochemical and photocatalysis experiments. a–c) Photoelectrical cell characterization. a) Cell configuration, where the ENZ catalyst is used as the working electrode in a one-compartment cell with a buffer (pH) electrolyte. The sample is illuminated using white light under different potentials. b) Current-time trace at –0.1 V versus reversible hydrogen electrode potential. The negative photocurrent is indicative of the cathodic nature of the ENZ catalyst. c) Photoelectrochemical external quantum efficiency (PEQE) spectra, which follow a Fowler emission model for the emission of ENZ plasmonically derived hot carriers over the TiO_2–Pd Schottky barrier. d–f) Photocatalysis characterization. d) Reactor cell for the characterization of the ENZ structure as an autonomous photocatalyst. The electrolyte consists of a 0.8:0.2 (v/v) mixture of water and methanol, where the latter is used as a hole-scavenger sacrificial agent. Samples are excited with AM 1.5G simulated illumination. e) Amount of H_2 evolved at different times with (blue) and without (black) a 450 nm long-pass filter for light, showing a stable generation of 7.5 μmol cm^{-2}. f) Comparison of H_2 generation rates for full-spectrum illumination with a flat sample and nanorod plasmonic photocatalysts.

(Figure 3d). Photogenerated electrons react with water and drive H_2 evolution, whereas the generated holes diffuse to uncovered Pd and oxidize MeOH as the sacrificial agent. To validate experimental results with theoretical predictions, we first characterized the H_2 evolution rate by employing a 450 nm long pass filter (Figure 3e). The amount of H_2 generated was periodically analyzed via gas chromatography (see the Experimental Section). The system achieve a constant H_2 evolution rate of 7.5 μmol h^{-1} cm^{-2} throughout the course of a 24 h interval (Figure 3f). The evolution rate under full solar illumination increases up to 9.5 μmol h^{-1} cm^{-2}, corresponding to an average quantum yield over the solar spectrum of ≈0.8%. The enhanced performance of this system is approximatively one order of magnitude higher than the quantum yield of 0.1% reported for plasmonic materials, in good agreement with our enhancement calculations in the previous text. The performance increase is mostly driven by light wavelengths >450 nm, as predicted by our calculations. Figure S9 in the Supporting Information reports experimental results over 50 h of measurements, showing a stable production rate of hydrogen from the ENZ photocatalyst unit.

In this work we demonstrated a complex epsilon-near-zero Pd/TiO_2/Pt metamaterial catalyst for efficient H_2 production. The reported quantum conversion efficiency of 0.8% represents a 3.2-fold improvement compared to best metal-sensitized hot-carrier photocatalyst for H_2 dissociation reported to date.[20] The superior performance of this approach stems on the broadband light-squeezing effect achieved by the 3D ENZ metamaterial. Using electron energy loss spectroscopy, we proved imaged hot carrier generation revealing a broadband localized generation in sub 10 nm dimensions. The catalyst shows a remarkable H_2 production rate of 9.5 μmol h^{-1} cm^{-2}, stable over the course of an initial 50 h study. Further optimization can be envisaged by their integration with oxygen-evolution catalysts such as cobalt.[3] Increase in the catalytic activity is expected by optimizing, or even suppressing, the barrier with the wide-bandgap semiconductor in such a way the ENZ metamaterial could directly drive chemical reactions.[24] The versatile nature of the ENZ material can also open applications for the production of other chemical fuels in different Pd based redox reactions, which can benefit from the optimized mechanism of hot-electrons generation developed herein.

Experimental Section

ENZ-Photocatalytic Device Fabrication: The ENZ materials were fabricated through an electroplating process using $HAuCl_4$ (99.99%

Sigma Aldrich) and HCl (TraceSELECT) solutions. The procedure was carried out by employing three electrode configuration in which the working electrode was connected with gold-coated substrates (1 cm^2) (EMF Corporation); the counter electrode was connected to a platinum mesh electrode; and the reference electrode is Ag/AgCl reference electrode. The fractal disorder metallic structures were formed in the 100×10^{-3} M L^{-1} concentration $HAuCl_4$ at −300 mV for 300 s. The 30 nm Pd layer was grown on the prepared disorder Au substrates through E-beam evaporation method. Then the 90 cycles (8 nm) TiO_2 film was conformally coated on top sample by ALD at low temperature condition. Then $TiCl_4$ treatment was applied to ENZ samples. The Pt cocatalysts loading was performed using light-assisted electroplating method in 20 µmol L^{-1} $HPtCl_4$ (Sigma Aldrich) at −600 mV for 600 s.

Spectrophotometer Measurements: Absorption measurements were carried out using a Perkin-Elmer Lambda 950 UV–Vis–NIR spectrophotometer equipped with an integrating sphere. Samples were placed at the center of the integrated sphere tilted at an angle of 20° relative to the incident beam. The total transmission (T) and reflectance (R) were collected by the integrating sphere detector with all ports closed except the one for the incident beam. Absorption was calculated as $100\% - T - R$. The 100% transmission baseline measurement was an empty sphere.

Transmission Electron Microscopy and Electron Energy Loss Spectroscopy Study: The samples for TEM studies were prepared by FIB (Helios 650, FEI). The authors first dispersed the metallic tree-like needles on the surface of a silicon substrate, then picked up one of them and spliced the thicker end of the needle to a FIB lift-out grid. This sample preparation method ensures that the network of ENZ structures used for surface plasmon mapping is electrically insulated to the ambient environment. The STEM EELS spectrum imaging (SI) measurement was carried out using the Titan G2 60-80 (FEI) equipped with a monochromator, a spherical aberration corrector, and a high energy resolution Gatan imaging filter system. All SI measurements were carried out in monochromatic mode and the energy resolution of incident beam was estimated to be 0.14 eV. The spectrometer dispersion was set to 0.01 eV, and the persistence time was 0.05 s for each spectrum. Plasmon maps were obtained from a 0.2 eV EELS intensity window.

Material Characterization: The SEM images of Au samples were acquired using a Hitachi SU8230 scanning electron microscope operated at 1.0 kV. TEM, high resolution TEM images, high-angle annular dark-field STEM, and STEM elemental mapping for the samples were taken on a HF-3300 transmission electron microscope operated at 200 kV. The samples were prepared by dropping catalyst powder dispersed in ethanol onto carbon-coated copper TEM grids (Ted Pella, Redding, CA) using micropipettes and were dried under ambient conditions.

Photocatalyst Characterization for Hydrogen Evolution: The ENZ active material was deposited into a defined 0.8×0.8 cm^2 area. The photocatalytic reactions were carried out in a gas-tight 30 mL Pyrex reaction cell at ambient temperature and atmospheric pressure under simulated AM 1.5G solar illumination. The source intensity was measured using a Melles–Griot broadband power meter and a Thorlabs broadband power meter through a circular 0.049 cm^2 aperture at the position of the device. In a typical photocatalytic experiment, photocatalyst substrates were vertically located in the reactor filled with 15 mL of aqueous solution containing 20% (v/v) of methanol. The mixture was evacuated and purged with nitrogen for 30 min to remove dissolved oxygen. Then, it was illuminated with a solar simulator equipped with an UV-cutoff filter (450 nm) (for testing under visible light) for different periods of time. A 0.5 mL of gas was sampled intermittently through the septum, and hydrogen was analyzed by gas chromatography equipped with thermal conductivity detector (TCD) detector and carboxen-1010 capillary column. The system was calibrated periodically between measurements. The quantum yield (QY) was calculated according to following equation

$$\mathrm{QY} = \frac{\text{Number of reacted electrons}}{\text{Number of incident photons}} \times 100 = \frac{\text{Evolved } H_2 \text{ molecules} \times 2}{\text{Number of incident photons}} \times 100 \quad (2)$$

The number of incident photos was calculated by integrating the entire AM 1.5G spectrum between time 0 and the sampling time. At each iteration the head-space gas volume was corrected by the amount of the removed sample (0.5 mL).

The spectral response of the ENZ photocatalyst was acquired by illuminating the sample with 20 Hz chopped light and reading the photocurrent with a Stanford SR830 lock-in amplifier in a three-electrode configuration. A bias of −0.1 V versus reversible hydrogen electrode potential was applied to the sample using a Keithley 2400 source measuring unit. The cathodic nature of the photocurrent was recorded under the same conditions, where the light was manually modulated and the photocurrent directly recorded with the Keithley. Power calibration was performed by measuring the power of the incident monochromatic, obtained by passing a 400 W Xe lamp through a monochromator with appropriate cutoff filters. The output power was recorded with Newport 818-UV and Newport 838-IR photodetectors.

Supporting Information

Supporting Information is available from the Wiley Online Library or from the author.

Acknowledgements

Y.T. and F.P.G.d.A. contributed equally to this work. For the computer time, the authors used the resources of the KAUST Supercomputing Laboratory and the Redragon cluster of the Primalight group. This work was supported by KAUST (Award No. OSR-2016-CRG5-2995), the Ontario Research Fund-Research Excellence Program, the Natural Sciences and Engineering Research Council (NSERC) of Canada, and the Connaught Global Challenges program of the University of Toronto.

Conflict of Interest

The authors declare no conflict of interest.

Keywords

artificial photosynthesis, hot electron generation, hydrogen generation, photocatalysts

Received: February 28, 2017
Revised: March 26, 2017
Published online: May 8, 2017

[1] J. Liu, Y. Liu, N. Liu, Y. Han, X. Zhang, H. Huang, Y. Lifshitz, S. Lee, J. Zhang, Z. Kang, *Science* **2015**, *347*, 970.
[2] L. Liao, Q. Zhang, Z. Su, Z. Zhao, Y. Wang, Y. Li, X. Lu, D. Wei, G. Feng, Q. Yu, X. Cai, J. Zhao, Z. Ren, H. Fang, F. Robles-Hernandez, S. Baldelli, J. Bao, *Nat. Nanotechnol.* **2014**, *9*, 69.
[3] Q. Wang, T. Hisatomi, Q. Jia, H. Tokudome, M. Zhong, C. Wang, Z. Pan, T. Takata, M. Nakabayashi, N. Shibata, Y. Li, I. D. Sharp, A. Kudo, T. Yamada, K. Domen, *Nat. Mater.* **2016**, *15*, 611.
[4] M. W. Kanan, D. G. Nocera, *Science* **2008**, *321*, 1072.
[5] M. L. Brongersma, N. J. Halas, P. Nordlander, *Nat. Nanotechnol.* **2015**, *10*, 25.
[6] C. Clavero, *Nat. Photonics* **2014**, *8*, 95.
[7] N. J. Halas, S. Lal, S. Link, W. S. Chang, D. Natelson, J. H. Hafner, P. Nordlander, *Adv. Mater.* **2012**, *24*, 4842.

[8] S. Linic, P. Christopher, D. B. Ingram, *Nat. Mater.* **2011**, *10*, 911.
[9] M. W. Knight, H. Sobhani, P. Nordlander, N. J. Halas, *Science* **2011**, *332*, 702.
[10] F. P. García de Arquer, A. Mihi, D. Kufer, G. Konstantatos, *ACS Nano* **2013**, *7*, 3581.
[11] S. Mubeen, J. Lee, W. Lee, N. Singh, G. D. Stucky, M. Moskovits, *ACS Nano* **2014**, *8*, 6066.
[12] H. Chalabi, D. Schoen, M. L. Brongersma, *Nano Lett.* **2014**, *14*, 1374.
[13] K. Wu, J. Chen, J. McBride, T. Lian, *Science* **2015**, *349*, 632.
[14] Y. Tian, T. Tatsuma, *Chem. Commun.* **2004**, 1810.
[15] Y. Tian, T. Tatsuma, *J. Am. Chem. Soc.* **2005**, *127*, 7632.
[16] J. Lee, S. Mubeen, X. Ji, G. D. Stucky, M. Moskovits, *Nano Lett.* **2012**, *12*, 5014.
[17] S. Mukherjee, F. Libisch, N. Large, O. Neumann, L. V. Brown, J. Cheng, J. B. Lassiter, E. A. Carter, P. Nordlander, N. J. Halas, *Nano Lett.* **2012**, *13*, 240.
[18] S. Mubeen, J. Lee, D. Liu, G. D. Stucky, M. Moskovits, *Nano Lett.* **2015**, *15*, 2132.
[19] W. Xie, S. Schlücker, *Nat. Commun.* **2015**, *6*, 7570.
[20] S. Mubeen, J. Lee, N. Singh, S. Kramer, G. D. Stucky, M. Moskovits, *Nat. Nanotechnol.* **2013**, *8*, 247.
[21] G. V. Hartland, *Chem. Rev.* **2011**, *111*, 3858.
[22] P. Narang, R. Sundararaman, H. A. Atwater, *Nanophotonics* **2016**, *5*, 96.
[23] H. Harutyunyan, A. B. F. Martinson, D. Rosenmann, L. K. Khorashad, L. V. Besteiro, A. O. Govorov, G. P. Wiederrecht, *Nat. Nanotechnol.* **2015**, *10*, 770.
[24] A. O. Govorov, H. Zhang, Y. K. Gun'ko, *J. Phys. Chem. C* **2013**, *117*, 16616.
[25] R. Sundararaman, P. Narang, A. S. Jermyn, W. A. Goddard III, H. A. Atwater, *Nat. Commun.* **2014**, *5*, 5788.
[26] L. V. Besteiro, A. O. Govorov, *The J. Phys. Chem. C* **2016**, *120*, 19329.
[27] F. P. García de Arquer, A. Mihi, G. Konstantatos, *ACS Photonics* **2015**, *2*, 950.
[28] M. G. Silveirinha, N. Engheta, *Phys. Rev. B* **2007**, *76*, 245109.
[29] M. Silveirinha, N. Engheta, *Phys. Rev. Lett.* **2006**, *97*, 157403.
[30] A. Alù, M. G. Silveirinha, A. Salandrino, N. Engheta, *Phys. Rev. B* **2007**, *75*, 155410.
[31] R. Maas, J. Parsons, N. Engheta, A. Polman, *Nat. Photonics* **2013**, *7*, 907.
[32] E. J. R. Vesseur, T. Coenen, H. Caglayan, N. Engheta, A. Polman, *Phys. Rev. Lett.* **2013**, *110*, 013902.
[33] A. Giugni, B. Torre, M. Francardi, M. Malerba, A. Alabastri, R. P. Zaccaria, M. I. Stockman, E. D. Fabrizio, *Nat. Nanotechnol.* **2013**, *8*, 845.
[34] J. Huang, C. Liu, Y. Zhu, S. Masala, E. Alarousu, Y. Han, A. Fratalocchi, *Nat. Nanotechnol.* **2015**, *11*, 60.
[35] H. Galinski, G. Favraud, H. Dong, J. S. T. Gongora, G. Favaro, M. Dobeli, R. Spolenak, A. Fratalocchi, F. Capasso, *Light: Sci. Appl.* **2017**, *6*, e16233.
[36] A. Vakil, N. Engheta, *Science* **2011**, *332*, 1291.
[37] J. Pendry, A. Aubry, D. Smith, S. Maier, *Science* **2012**, *337*, 549.
[38] U. Leonhardt, *Science* **2006**, *312*, 1777.
[39] L. Soleymani, Z. Fang, B. Lam, X. Bin, E. Vasilyeva, A. J. Ross, E. Sargent, S. O. Kelley, *ACS Nano* **2011**, *5*, 3360.
[40] E. Vasilyeva, B. Lam, Z. Fang, M. D. Minden, E. Sargent, S. O. Kelley, *Angew. Chem., Int. Ed.* **2011**, *50*, 4137.
[41] B. Schaffer, W. Grogger, G. Kothleitner, F. Hofer, *Ultramicroscopy* **2010**, *110*, 1087.
[42] C. Colliex, M. Kociak, O. Stéphan, *Ultramicroscopy* **2016**, *162*, A1.
[43] S. A. Maier, *Plasmonics: Fundamentals and Applications*, Springer, London, UK **2007**.
[44] M. Bernardi, J. Mustafa, J. B. Neaton, S. G. Louie, *Nat. Commun.* **2015**, *6*, 7044.
[45] C. Liu, A. D. Falco, D. Molinari, Y. Khan, B. S. Ooi, T. F. Krauss, A. Fratalocchi, *Nat. Photonics* **2013**, *7*, 473.
[46] C. Liu, R. E. C. Wel, N. Rotenberg, L. Kuipers, T. F. Krauss, A. D. Falco, A. Fratalocchi, *Nat. Phys.* **2015**, *11*, 358.
[47] M. L. Coluccio, F. Gentile, G. Das, A. Nicastri, A. M. Perri, P. Candeloro, G. Perozziello, R. P. Zaccaria, J. S. T. Gongora, S. Alrasheed, A. Fratalocchi, T. Limongi, G. Cuda, E. D. Fabrizio, *Sci. Adv.* **2015**, *1*, e1500487.
[48] S. Adachi, *The Handbook on Optical Constants of Metals*, World Scientific, London, UK **2012**.

